A SAXS outlook on disordered carbonaceous materials for electrochemical energy storage

Damien Saurel, Julie Segalini, María Jauregui, Afshin Pendashteh, Barbara Daffos, Patrice Simon, Montse Casas-Cabanas

Energy Storage Materials 21 (2019) 162–173

Contents lists available at ScienceDirect

Energy Storage Materials

journal homepage: www.elsevier.com/locate/ensm

A SAXS outlook on disordered carbonaceous materials for electrochemical energy storage

Damien Saurel [a,**], Julie Segalini [a], María Jauregui [a], Afshin Pendashteh [a], Barbara Daffos [b,c], Patrice Simon [b,c], Montse Casas-Cabanas [a,*]

[a] CIC Energigune, Parque Tecnológico de Álava, Albert Einstein 48, Ed. CIC, 01510, Miñano, Spain
[b] Réseau sur le Stockage Electrochimique de l'Energie (RS2E), FR CNRS, 3459, France
[c] CIRIMAT, Université Toulouse, CNRS, INPT, UPS, 31062, Toulouse, France

ARTICLE INFO

Keywords:
Disordered carbons
Small angle X-ray scattering
Battery
Supercapacitor
Pore structure

ABSTRACT

Ordered and disordered carbonaceous materials cover a wide range of the energy storage materials market. In this work a thorough analysis of the Small Angle X-ray Scattering (SAXS) patterns of a number of carbon samples for energy storage (including graphite, soft carbon, hard carbon, activated carbon, glassy carbon and carbide-derived carbon) is shown. To do so, innovative geometrical models to describe carbon X-ray scattering have been built to refine the experimental SAXS data. The results obtained provide a full description of the atomic and pore structures of these carbons that in some cases challenge more traditional models. The correlative analysis of the descriptors here used provide novel insight into disordered carbons and can be used to shed light in charge storage mechanisms and to design improved carbonaceous materials.

1. Introduction

Carbonaceous materials cover a very large family of structures and textures that span a wide range of unique chemical and physical properties. The number of carbon forms that can be created by the choice of the carbon precursor and by controlling the carbonization process is extremely large, and research on carbon-based materials is a very dynamic and growing area of study with nearly unlimited possibilities [1]. Owing to their unique versatility, carbon materials also represent a key family of materials in the field of electrochemical energy storage. Their low cost, high electrical conductivity and the myriad of nano- and micro-textural arrangements and surface functionality make them suitable to most relevant energy storage technologies: supercapacitors [2], Li/Na/K-Ion Batteries [3–5], Li-S [6] and Metal-air batteries [7–9].

Carbon sp^2 allotropes are typically represented by graphite, in which the layers of carbon hexagons are stacked in parallel. Graphite usually crystallizes as a mixture of the hexagonal 2H (ABABAB graphene layer stacking) and rhombohedral 3R (ABCABC graphene layer stacking) polytypes and is commonly described by giving the relative fractions of 2H, 3R and turbostratic stacking (i.e. graphitic planes are still parallel but shifted or rotated). Graphite (natural and synthetic) can be considered as the standard negative electrode in the lithium-ion battery technology and is yet, by far, the most commercially used. The maximum lithium uptake of graphite is LiC_6 (with 372 mA h g^{-1} and 975 mA h cm^{-3} gravimetric and volumetric capacity) and is concomitant to a transformation to AAAA stacking [3,10].

Disordered carbon materials like soft and hard carbons can also be lithiated to a certain extent, but the amount of lithium reversibly incorporated in the carbon lattice, the faradaic losses during the first cycle and the profile of the potential composition profile can exhibit some differences [3,11,12]. Soft carbons are graphitizable carbons that have been calcined below graphitization temperature (typically 2500 °C). These carbons, at temperatures around 1000 °C, tend to form parallel stacked graphene layers though with a high degree of defects (dislocations, curvature, and tilt). Soft carbons are thus fully turbostratic and owe their designation to the weakness of the layer to layer bonds that provides mechanical softness at ambient temperature [13–15].

Conversely, hard carbons are non-graphitizable and do not exhibit a long-range ordered structure. Hard carbons are commonly obtained by precursors presenting strongly cross-linked structures that do not allow for the ordering of the layers, and forbid the densification of the carbon structure and induce the formation of microporosity as a consequence of

* Corresponding author.
** Corresponding author.
E-mail addresses: dsaurel@cicenergigune.com (D. Saurel), mcasas@cicenergigune.com (M. Casas-Cabanas).

https://doi.org/10.1016/j.ensm.2019.05.007
Received 18 February 2019; Received in revised form 6 May 2019; Accepted 6 May 2019
Available online 15 May 2019

gas evolution upon the release of heteroatoms [16,17]. Their structure is typically described by discrete fragments of graphenic sheets that are locally stacked (with no more than a few layers in the stacking direction) in a highly turbostratic layered structure, that at a larger scale result in voids and pores [4,16,18].

Petroleum coke is the typical precursor for synthetic graphite, and Calcinated Petroleum Coke (CPC) calcined at temperatures below graphitization was used in the first generation of Li-ion cells [19], which was later replaced by HC to increase the energy density, and later by graphite once the solvent co-intercalation issue was circumvented [20]. On the other hand, since the electrochemical insertion of sodium ions into graphite is limited as occurs below the sodium plating voltage [21,22], hard carbon is the most studied sodium ion negative electrode [4], able to reversibly react with a typical sloping voltage–composition curve below 1 V vs Na^+/Na and a low voltage plateau below 100 mV vs Na^+/Na [23,24], exhibiting capacities that reach 350 mA h g^{-1} [25].

Glassy carbons in turn are obtained at higher temperatures (≈ 3000 °C) and with a slow heat treatment. Their properties are similar to inorganic glasses, with black colour and perfectly smooth surfaces, and their main feature is a high closed micropore volume inaccessible to any adsorbent including helium, leading to an exceptional chemical inertness [14,26]. The use of glassy carbon as active material is rather limited for electrochemical energy storage application, although it has recently attracted attention as Na-ion anode as its reaction voltage is very low (lower than 50 mV) and capacities of up to 200 mA h g^{-1} have been reported [27].

On the contrary, if the char is oxidized or activated using an agent such as steam or carbon dioxide, or chemicals like KOH or H_3PO_4, micropores can be created (pore size <2 nm) resulting in a very high surface area [28]. The final result is a disordered carbon with an open pore structure with a wide pore size distribution. Activated carbons are used in a large number of applications and thanks to their very low cost have been successfully implemented in electrochemical double layer capacitors (EDLC) for charge storage [2,29]

Carbide Derived Carbons (CDCs) have also been widely explored as EDLC electrode materials [2,30,31]. CDCs are microporous carbons with a very narrow pore size distribution. They are produced from high-temperature etching of metal carbides (TiC, SiC and VC among others) under chlorine gas atmosphere or vacuum deposition [2]. Contrary to all the other carbons studied here, whose precursors are typically rich in sp^2 hybridization, CDCs precursors are 100% sp^3. However, sp^3 carbon is metastable in absence of H or heteroatoms so that transition to sp^2 is expected to occur with heat treatment. Indeed, although highly crystalline sp^3 (diamond) structure transformation into sp^2 graphite does not occur below 1700 K, in the case of amorphous diamond like carbons, sp^3 to sp^2 transition occurs near 500 °C [26,32]. It is therefore likely that low temperature CDCs exhibit a non-negligible amount of sp^3 carbons, whose amount decreases with synthesis temperature.

The electrochemical properties of the different carbon textures described above are strongly influenced by macro- and micro-structural features, that include the specific surface, surface chemistry, morphology, crystallinity and orientation of the graphene layers as well as their pore structure. The intensive research aimed at developing carbonaceous materials with optimized performance has resulted in a deep understanding of some of the key factors that control carbon's electrochemical performance. However, despite recent valuable efforts, the disordered character of many of the carbon textures described above, together with the difficulties of reliably uncoupling pore size and pore accessibility still represent a characterization challenge [2]. Particular microstructural features of carbonaceous materials are locked by the limitations of conventional analytical techniques such as gas adsorption (no access to buried pores, analysis requires pore geometry assumptions), X-ray diffraction (XRD, lack of long-range order) or Transmission Electron Microscopy (TEM, lack of contrast), to name a few. The result is an uncomplete or simplified description of carbon structure and microstructure that is partly responsible for the lack of consensus on charge storage mechanisms [4]. Indeed, traditional models to describe the short and long range carbon structures are based on the assumption that their microstructure is made of an assembly of pseudo graphitic nanocrystals [16], as represented in Fig. 1, left panel. These nanocrystals would be randomly tilted (although approximately parallel to each other) in soft carbons. In hard or non-graphitizable carbons they would be cross-linked (either through amorphous regions or sp^3 bonded carbons, which would explain the non-graphitizability) and randomly oriented, creating voids. Such interpretation relies on the assignment of the XRD peak width only to crystallite size broadening and is still largely used to describe the charge storage mechanism in hard carbons, see e.g. Refs. [4,18,33,34]. However, this model has been recently challenged, and alternative models have been proposed based on curved layers (right panel of Fig. 1) [26,35–38]. This curvature is made stable under heat treatment by the presence of non-hexagonal rings in the graphene layers, similarly to fullerene derivates, forbidding the graphitization and maintaining the micropore structure [26,39]. Layer curvature is a potential source of peak broadening that should be accounted for together with (or instead of) limited crystallite size [40].

In this paper we use Small Angle X-ray Scattering (SAXS) to thoroughly study the structure of different types of carbons at multiple length scales. SAXS offers several advantages over other techniques as is able to provide topological information from the molecular-to the meso-scale regardless of the sample crystallinity, and allows including non-traditional descriptors for porosity. In order to describe the complex structure of disordered carbons and extract averaged quantitative information from scattered intensities, innovative geometrical models to describe carbon X-ray scattering have been built and the experimental SAXS data have been refined using these models. The obtained results provide an accurate description of disordered carbons that we believe will be of high value to orient future research for their optimization.

2. Material and methods

2.1. Samples

Synthetic graphite (graphite hereafter), calcined petroleum coke (CPC) and active carbon (AC) are commercial powder samples from Imerys (graphite and CPC) and Kurarai (AC). Sugar based hard carbon powder sample (SHC) was prepared from the pyrolysis under argon at

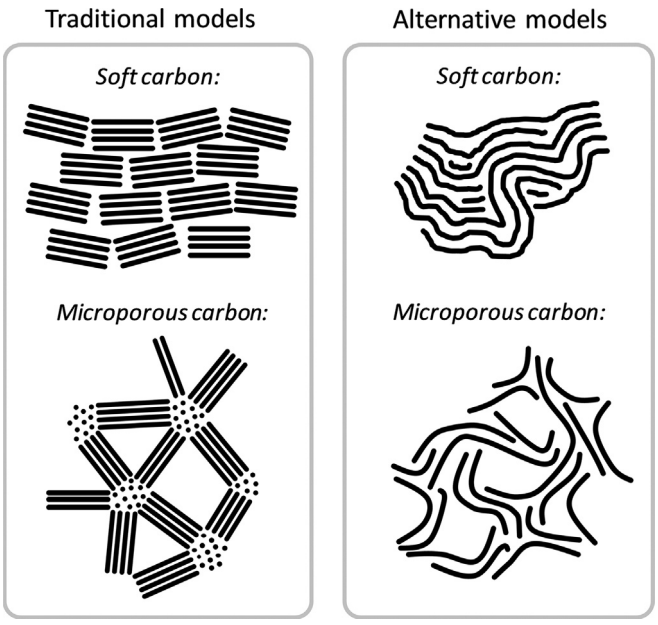

Fig. 1. Schematic view of traditional and alternative models for soft carbon and microporous carbon.

1050 °C for 12 h of dewatered sucrose, followed by hand grinding. Dewatering of sucrose (Sigma-Aldrich) was performed by heating in air at 160 °C for 24 h. Carbide derived powder carbon samples were provided by Y-Carbon company, CDC400 and CDC900 hereafter, according to their chlorination temperature (400 °C and 900 °C, respectively). The glassy carbon (GC) sample was provided by Bruker company. GC sample had the shape of a parallelepiped with square section of 30 mm × 30 mm and thickness of 2 mm, with the aspect of a black and opaque glass with polished surfaces, see Fig. S3.

2.2. Powder X-ray diffraction

Powder X-ray diffraction patterns were measured using a Bruker D8 diffractometer, using either Cu or Co K-α source, and LYNXEYE detector in the Bragg-Brentano reflection geometry. Monocrystalline Si sample holders with shallow cavity have been used to avoid any background signal coming from the sample holder.

2.3. Scanning electron microscopy

Scanning electron micrographs were collected with a FEI Quanta 200 SEM microscope equipped with a Field Emission electron gun and ET detector, running at an accelerating voltage of 20 kV and a spot size of 3.5 nm. Size analysis of the particles was carried out using the ImageJ software with a minimum particle population of 20.

2.4. Gas adsorption

Nitrogen Adsorption/desorption isotherms were acquired at 77 K using a Micromeritics ASAP 2020 for samples preliminarily outgassed for 8 h at 200 °C. The Specific Surface Area (SSA) values were calculated using the B.E.T. method.

2.5. Small angle X-ray scattering

Small Angle X-ray Scattering (SAXS) was performed using a Bruker Nanostar instrument, composed of a Cu K-α source, three pinhole collimators, evacuated beam path and a Vantec 2000 2D detector of active surface area 14 mm × 14 mm and 2048 × 2048 pixels, see Fig. 2 (upper panel) for a schematic representation. Transmission geometry is used, and the detector plane is perpendicular to the beam axis and centred on the same. The intensity is then integrated angularly on all the detector surface and normalized to units of counts per second (cps) per pixel. Several corrections need to be made on the raw data before and after angular integration, related to distortions and other factors correlated to the experiment geometry and detector's working principle. A review of all the data corrections that need to be done can be found in e.g. Ref. [41], and the detail on the corrections made for the present study can

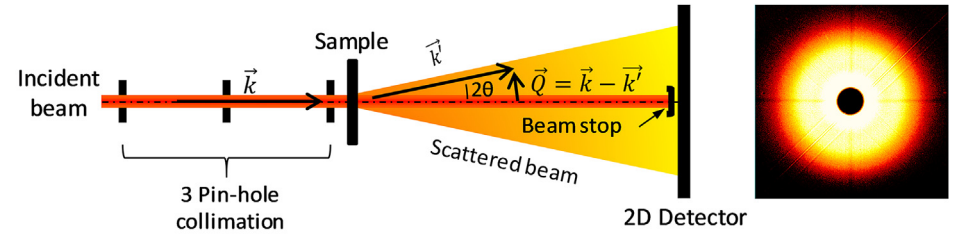

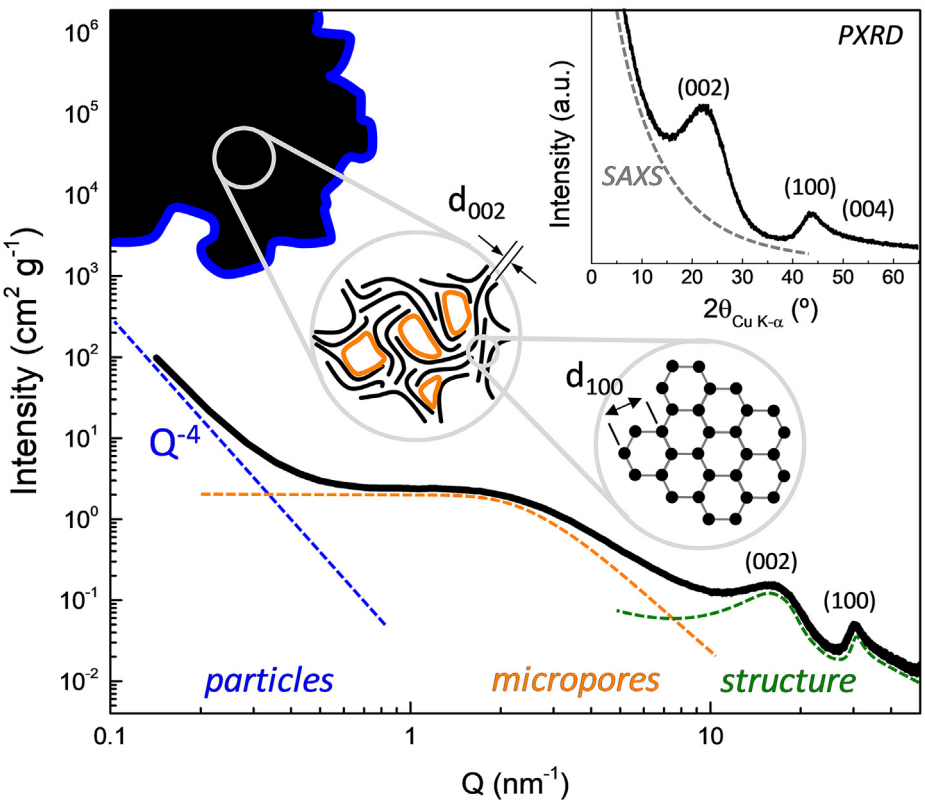

Fig. 2. Top panel: schematic representation of the geometry of the SAXS instrument used for the present study. Bottom panel: typical intensity versus scattering vector curve in log-log scale of a microporous non-graphitic carbon, together with schematic drawing of the structural, microstructural and morphological features that are related to the intensity observed in the large, intermediate and low Q ranges, respectively. Inset: linear scale representation of the same pattern vs the scattering angle 2θ as it is usually done for PXRD patterns.

be found in Annex 1.

A nickel foil was used to filter out K_β from the Cu tube source. Three sample to detector distances have been used, 107 cm, 28 cm and 6 cm, to cover a broad angular range (0.1–30 nm^{-1} in scattering vector Q values). The instrument has been calibrated for absolute intensity (see Annex 1 for more details), flat field (relative pixel to pixel detector's efficiency) and spatial distortion. Distance calibrations were performed at all distances using silver-behenate (107 and 28 cm) or corundum (5 cm) as reference. Since all samples generated an isotropic intensity pattern at all sample-detector distances, angular integration over the whole detector surface was performed to extract intensity evolution with scattering angle. The measured intensity has then been corrected for all the relevant factors including sample transmission, and the intensity calibrated, see Annex 1 for more details. The scattering from the sample holder, when used, has been subtracted. Powder samples were gently compacted in 4 × 4 mm circular cavities of a 1.5 mm thick steel plate and held in place by two tape sheets. In this case an empty cavity with two tape sheets was measured as a blank for the sample holder scattering signal.

A schematic representation in log-log scale of the typical scattering pattern of a powder material presenting microstructural features is shown in the lower panel of Fig. 2. In general terms the exponent n of the Q^{-n} behaviour (linear behaviour in log-log scale) is morphology dependent and inflexion points allow determining characteristic sizes, while the intensity depends on the scattering contrast and amount of specific surface area. Since a SAXS pattern covers a very wide length scale, morphological information can be extracted from most possible microstructural features. Three main contributions to the intensity can be observed in Fig. 2: i) A slope in Q^{-4} at low angle, which corresponds to the Porod's law of scattering by sharp interfaces, that can be ascribed to the macroscopic surface area of the powder grains (I_{Porod} hereafter); ii) Diffraction peaks in the wide-angle limit (WAXS) which are related to the carbon's structure (I_{waxs} hereafter); and iii) a signal in the intermediate Q range caused by microporosity whose profile depends on its nature (I_{mp} hereafter). The intensity can thus be modelled by the combination of three terms:

$$I^{cm^2 g^{-1}} = I_{Porod} + I_{mp} + I_{waxs} \quad (1)$$

The theoretical models used for refining the full range SAXS intensity are presented in the next section, and more details can be found in Annex 2. All experimental data refinements were done using the non-linear curve fit functionality of OriginPro software, using Levenberg–Marquardt algorithm, and in logarithmic scale in order to confer equivalent weight to the whole pattern, as intensity can span over several orders of magnitude.

3. Results

In this section the full range SAXS-WAXS patterns of different carbons is analysed. To do so, the samples are divided into three groups: non-porous, microporous and carbide-derived carbons. Structural and morphological models have been built to provide a general description of the particularities of each type of carbon and, following the calibration of scattered intensities, experimental data have been refined in order to obtain quantitative information of relevant structural and microstructural descriptors. A brief description is given for the built models corresponding to each of the contributions to the scattered intensity (I_{waxs}, I_{mp}, I_{Porod}, see Annex 2 for a full description) and the full range refinement of structural and morphological parameters is subsequently shown. Finally, a general discussion is provided from the comparison of the obtained data.

3.1. Structural model for the disordered turbostratic structure (I_{waxs})

Traditional structural determination methods based on the analysis of powder X-ray diffraction data such as the Rietveld method cannot be directly applied for the characterization of disordered carbons. Indeed, diffraction peaks are typically strongly broadened owing to the lack of crystallinity arising for example from their turbostratic character. Some insight, however, can be accessed from the analysis of peak shapes, in particular that of the main interlayer peak, by using the theory developed for disordered or distorted lamellar phases in polymer science. Indeed, a lamellar ordered arrangement of at least two phases with distinct scattering length density will give rise to a diffraction peak:

$$I_{waxs} = K\frac{P_{1D}}{Q^2} \cdot L(Q_c, w_L) \otimes G(Q_c, w_G) \cdot \exp\left(-Q^2\langle \delta z^2 \rangle/3\right) \quad (2)$$

where K is an intensity scaling factor and $Q_c = 2\pi/d$ is the centre of the peak, d being the periodicity. P_{1D} is the form factor of the layers, which is divided by Q^2 to average over all possible orientations of the structure (equivalent to powder averaging). $L \otimes G$ is the Voigt peak profile that is the convolution of a Lorentzian (L) and a Gaussian (G) peak functions, w_L and w_G being their respective full width at half maximum. Distortions that affect the long-range order, such as bends, cause Lorentzian broadening [40]. As discussed in Annex 3, a finite crystallite size broadening can be simulated by a Voigt-type profile with w_L/w_G ratio close to 1:2. Finally, the last factor accounts for local distortions of the structure that do not affect the long range order, such as local fluctuations of interlayer distance $\langle \delta z^2 \rangle$, either due to temperature (Debye-Weller factor) or structural disorder [40]. If this model is extrapolated to the (002) peak of the layered structure of sp^2 carbons, the two phases would be the graphene sheets and the interlayer space between them. The smooth transition from one phase to the other due to the spatial extension of the electron cloud of the graphene sheets is then taken into account by considering P_{1D} to be the atomic form factor of carbon atoms, which is tabulated and can be found e.g. in Ref. [31], the peak position Q_c would be defined as $2\pi/d_{002}$, and the parameters w_L, w_G and $\langle \delta z^2 \rangle$ would be related to the source of the crystallinity loss. As discussed in the Annex 3, an interesting feature of Lorentzian peak broadening is that intensity does not vanish at low angle, causing a Q^{-2} behaviour at low angle in combination with the orientation averaging factor. This can be seen from the simulations of Fig. 3a of three possible sources of peak broadening, schematically represented in Fig. 3b: nanocrystallites, bent layers and crumpled layers, i.e. presenting a large dispersity of curvature radius, see Annex 3 for more details. Nanocrystallites would cause a squared sinc peak function (discontinuous line in Fig. 3a) which can be approximated by a Voigt function with major Gaussian weight ("nano" in Fig. 3a), bent layers and crumpled layers would both result in a Lorentzian peak function (continuous curves in Fig. 3a). The extension of the peak would be in Q^{-2} for bent layers, and $Q^{\approx -2.5}$ for crumped layers. It can be seen from Fig. 3a that the narrower Lorentzian component in the case of nanocrystallites induces a less intense Q^{-2} SAXS signal compared to the 100% Lorentzian peak used to simulate bent layers. On the other hand, the crumpled layers display a more intensse SAXS signal due to the increase of the exponent n in Q^{-n} from 2 to 2.5. Extending the analysis to the lower angle can thus allow a more accurate discrimination between the source of peak broadening, size or curvature. In the latter case the Q dependency indicates if the layers are smoothly bent or if they are crumpled.

3.2. Particles morphological model (I_{Porod})

All the powder samples studied here exhibit particle sizes in the micrometre range (SEM images of Fig. S2 and Table S2). The smallest Q values studied here are close to 0.1 nm^{-1}, which is two orders of magnitude larger than the inverse of the size of the grains, therefore their contribution should only appear in the Porod's final slope [31], which is expected to show a Q^{-4} dependency according to expression (A3.7). Taking also into account that some surface roughness can exist in the mesoscopic range, the following expression has been used to simulate the low angle contribution I_{Porod}:

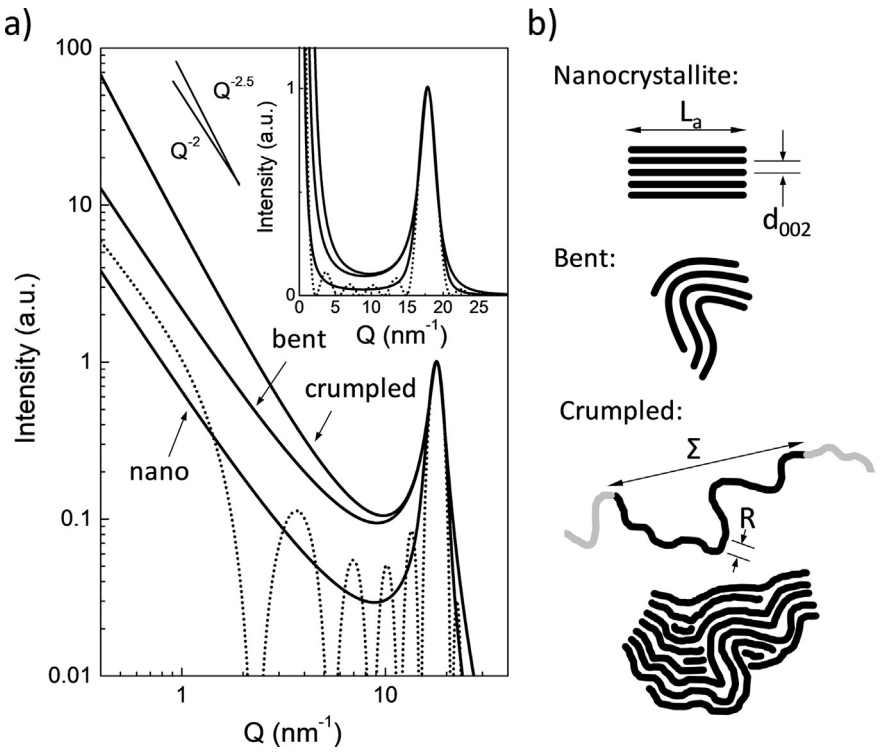

Fig. 3. a) Simulation of a (002) peak centred at $Q_c = 18\ \mathrm{nm}^{-1}$, a width of $5.6\ \mathrm{nm}^{-1}$ and considering three different sources of broadening: size broadening (square sinc – dotted line, and Voigt approximation), bent layers and crumpled layers (Lorentzian). Main panel in log-log scale, inset in linear scale. b) Schematic representation, from top to bottom, of nanocrystallites, stack of bent layers, stack of crumpled layers.

$$I_{Porod} = 2\pi(\Delta SLD)^2\left(S_{macro}Q^{-4} + S_{rough}\frac{\frac{2}{9}R_{rough}{}^4}{1+\frac{1}{5}(QR_{rough})^2+\frac{2}{9}(QR_{rough})^4}\right) \quad (3)$$

where S_{macro} is the macroscopic surface area of the grains of the powder, and S_{rough} the contribution to the surface area due to surface roughness. ΔSLD is the contrast of scattering length density between the powder grains and the vacuum that surrounds the sample, so that $\Delta SLD = SLD_{sample}$, whose value is given in Table S1 and has been calculated from the structural density ρ_{struc} according to expression (S1) using the NIST online tool [42], more details on the method can be found in supplementary information. For the mesoscopic surface roughness, the empirical form factor of globules has been used, normalized to 1 in the high Q limit, where R_{rough} can be interpreted as the characteristic size of the surface roughness. More details on this form factor can be found in annex 3. Note that for $Q \gg 1/R_{rough}$ expression (3) simplifies as a simple Porod's law:

$$I_{Porod} \underset{Q\gg\frac{1}{R}}{\longrightarrow} 2\pi(\Delta SLD)^2\left(S_{macro}+S_{rough}\right)Q^{-4} \quad (4)$$

3.3. Micropores morphological models (I_{mp})

In the low concentration limit the intensity scattered by pores would simply be the sum of the intensity scattered by all individual pores according to equation A2.7 (annex 2). However, some of the carbons studied in this work are known to exhibit a large (open or closed) porous volume, and therefore models for larger concentrations should be considered.

Increasing the concentration may have two distinct effects that are schematically represented in Fig. 4. If pores tend to agglomerate due to the presence of pore-pore correlations, as schematically represented in Fig. 4e, they will give rise to an additional contribution to the intensity in Q^{-D} at low angle, D being the fractal dimension of the aggregate, as represented in Fig. 4f. This can be modelized conveniently by considering a structure factor such as in expression (A2.20) of Annex 2:

$$I_{mp} = I_0\left(1+4\pi\frac{D}{4\pi r^D}\Sigma^D\frac{D\Gamma(D-1)}{\left(1+(Q\Sigma)^2\right)^{\frac{D-1}{2}}}\frac{\sin((D-1)\tan^{-1}(Q\Sigma))}{Q\Sigma}\right) \cdot\left(\exp\left(-(Qr)^2/5\right)+\left[\mathrm{erf}\left(\frac{Qr}{\sqrt{10}}\right)\right]^{12}\frac{9}{2}\frac{k}{(Qr)^4}\right) \quad (5)$$

$$I_0 = \frac{1}{\rho_{struc}}\phi(\Delta SLD)^2V_P^1 \quad (6)$$

where ρ_{struc} is the structural density calculated according to expression (S1), whose values are tabulated in Table S1, and ϕ the pore volume fraction. ΔSLD is the contrast of scattering length density between the pores and the sample's carbon matrix. Since the pores are empty voids, their SLD is zero so that $\Delta SLD = SLD_C$, whose value has been calculated for each sample from the structural density ρ_{struc} (more details on the method can be found in supplementary information). V_P^1 is the volume of an individual pore; for spheroid pores of radius r:

$$V_P^1 = \frac{4}{3}\pi r^3$$

The second factor of expression (5) is Teixeira's structure factor for fractal aggregates of dimension D [44], Σ being a cut-off length above which the correlation responsible of the fractal vanishes, see Annex 3 for more details. The third factor is the form factor of a particle with AR = 1 and average radius r. k is an adjustable factor that depends on the morphology: $k = 1$ for perfect spheres with narrow size distribution, $k > 1$ for globules of undefined shape. Here the unified fit approach has been used for the form factor, but the globule empirical form factor can be used as well with similar result. In case of slit pores, the form factor of a disc or discoid can be used. More details on these form factors can be found in Annex 3.

The specific surface area S_{mp} of the micropores can be determined from the equivalency of Porod's law with expression (5) in the high Q limit:

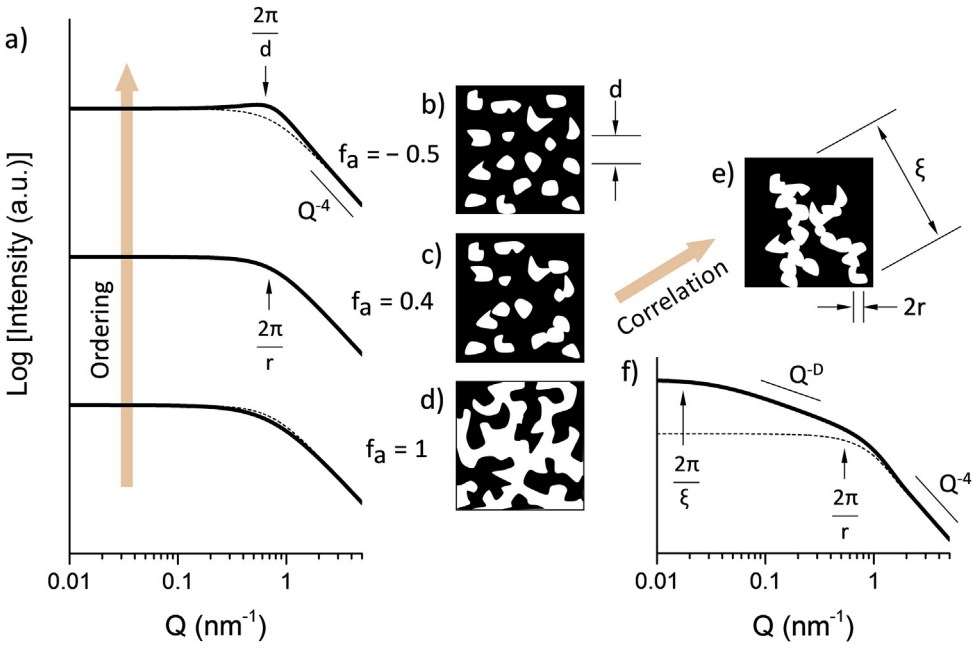

Fig. 4. a) SAXS simulations based on the Teubner-Strey model of two-phase mixtures of expression (7) with increasing ordering from bottom to top. The case corresponding to globules ($f_a = 0.4$) is represented as a discontinuous line for comparison on the top and bottom graphs. b-d) Schematic representations of the micropore arrangement corresponding to the three simulations of (a). e) Schematic representation of micropore clusters and (f) related SAXS signal based on the fractal aggregate model of expression (5) with fractal dimension $D = 1.5$.

$$S_{mp} = \frac{9k}{2r^4}\frac{I^0}{2\pi(\Delta SLD)^2} \tag{7}$$

If on the contrary pores tend to exhibit an average pore-pore distance, a broad peak will appear centred $Q_c = 2\pi/d$, d being the average pore-pore distance. In this case the system can be adequately modelized by the semi-empirical Teubner-Strey model which was initially derived for microemulsions [45,46]:

$$I_{mp} = I_0\frac{1}{1 + C_1Q^2 + C_2Q^4} \tag{8}$$

where I_0, C_1 and C_2 are adjustable parameters defined as:

$$I_0 = \frac{8\pi}{\rho_{struc}}\phi(\Delta SLD)^2\frac{\xi^3}{\left(1 + \left(\frac{2\pi\xi}{d}\right)^2\right)^2} \tag{9}$$

$$d = 2\pi\left[\frac{1}{2}C_2^{-\frac{1}{2}} - \frac{C_1}{4C_2}\right]^{-\frac{1}{2}} \tag{10}$$

$$\xi = \left[\frac{1}{2}C_2^{-\frac{1}{2}} + \frac{C_1}{4C_2}\right]^{-\frac{1}{2}} \tag{11}$$

where d is the pore-pore distance, and ξ a correlation length that limits the extension of the order.

The Teubner-Strey model considers a two-phase system, the two-phase having similar volume fraction, an average distance d between domains of the same phase, and a parameter f_a, called "amphiphilic factor" for microemulsions [45], which can be considered here as a disorder parameter:

$$f_a = \frac{C_1}{2\sqrt{C_2}} \tag{12}$$

As can be seen in Fig. 4a, for this model the intensity is constant in the low concentration limit, and falls as Q^{-4} in the large angle limit, in agreement with Porod's law. As represented in Fig. 4a, $f_a = 1$ corresponds to a totally disordered two-phase system, in which case the Teubner-Strey model is equivalent to the Debye-Bueche model for totally random two-phase systems [47]. For $f_a \approx 0.4$ the Teubner Strey model is equivalent to a particulate model of particles with AR close to 1, e.g. globules, see Annex 3 for more details. For smaller values of f_a, e.g. $f_a = -0.5$ in Fig. 4a, a broad peak appears centred at $Q_c = 2\pi/d$.

The pore volume fraction can be deduced from expression (A3.20) of annex 3:

$$\varphi = I_0\frac{\rho_{struc}}{8\pi(\Delta SLD)^2}\xi^{-3}\left(1 + \left(\frac{2\pi\xi}{d}\right)^2\right)^2 \tag{13}$$

The average pore radius r can be estimated by analogy with the globulus form factor defined in expression (A3.9):

$$r = \sqrt{5C_1} \tag{14}$$

Finally, the surface area can be estimated by analogy with the Porod's law as defined in expression (A3.7):

$$S_{mp} = \frac{I^0}{C_2 2\pi(\Delta SLD)^2} \tag{15}$$

3.4. Full range SAXS-WAXS analysis of graphite and CPC soft carbons

The full range SAXS experimental and fitted patterns of graphite and CPC samples are shown in Fig. 5. Only the contributions to I_{waxs} and I_{Porod} have been required to fit the data. The agreement between the model and the experimental pattern is very good for graphite, despite the intensity values are spread in nearly 6 orders of magnitude and more than two orders of magnitude are covered by the Q range. Moreover, it can be clearly observed that each of the two components of the model is preponderant in a different Q range, ensuring good precision in the determination of the refined parameters with low interdependence. All in all, the very good fit between the model and the full range SAXS pattern of the graphite sample denotes the total absence of microstructural features in the sub-mesoscopic range, such as micropores, which is to be expected as graphite is known to exhibit a dense and highly crystalline structure with long range order due to its very high temperature of synthesis (typically over 2500 °C). The refined values of the structural and morphological parameters related to I_{Porod} and I_{waxs} are presented in Table 1 and Table 2, respectively.

In the case of CPC soft carbon, a Q^{-n} dependency is observed in the intermediate Q range, $n \approx 2.5$, which indicates the presence of microstructural features not found in graphite. This exponent suggests a mass

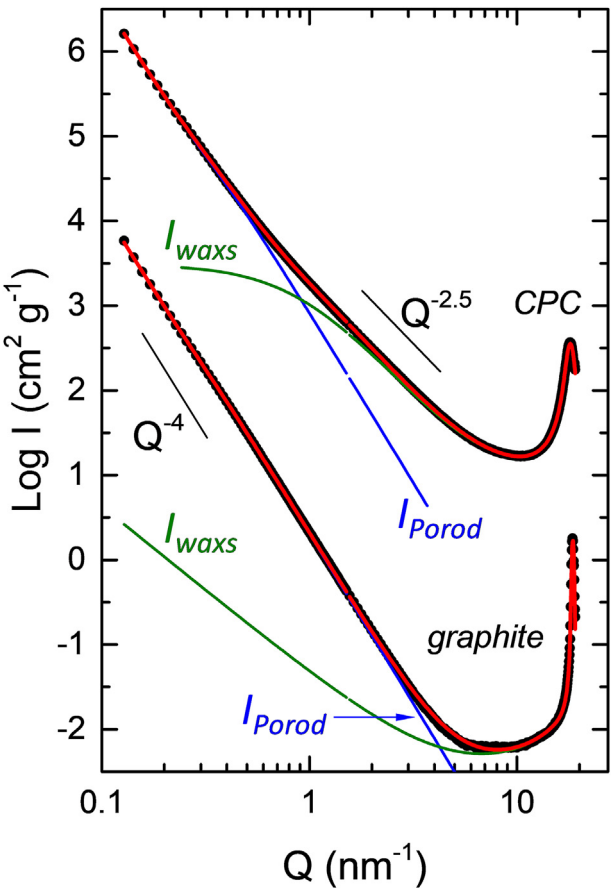

Fig. 5. Full range fit of non-porous carbons CPC and graphite. CPC intensity was shifted for clarity. Black round symbols represent the experimental data, red curve represents the calculated pattern, the blue curve corresponds to the calculated I_{Porod} and the green curve to the calculated I_{waxs}. (For interpretation of the references to colour in this figure legend, the reader is referred to the Web version of this article.)

fractal of dimension D ≈ 2.5, which is that of crumpled layers as discussed in Section 3.1 [48,49]. This is in agreement with early studies of non-graphitic calcined petroleum coke using HRTEM (high resolution transmission electron microscopy) which observed a disordered layered structure with a large degree of bends and curves [50]. Based on this observation, an additional structure factor (S_{3D}) to describe this feature has been needed in I_{waxs} expression (see annex 3 for more detail):

$$I_{waxs} = K \cdot \frac{S_{3D}}{Q^2} \cdot P_{1D} \cdot L \otimes G \cdot \exp\left(-Q^2\langle \delta z^2 \rangle/3\right) \quad (16)$$

$$\frac{S_{3D}}{Q^2} = \left(1 + 4\pi \frac{D}{4\pi r^D} \Sigma^D \frac{D\Gamma(D-1)}{\left(1+(Q\Sigma)^2\right)^{\frac{D-1}{2}}} \frac{\sin((D-1)\tan^{-1}(Q\Sigma))}{Q\Sigma}\right) \cdot \left(\exp\left(-(Qr)^2/6\right) + \left[\mathrm{erf}\left(\frac{1.06}{2\sqrt{3}} Qr\right)\right]^6 \frac{4}{(Qr)^2}\right) \quad (17)$$

Although the expression of S_{3D}/Q^2 is quite extensive, the number of refined parameters is limited to two characteristic distances Σ and r, in addition to the fractal dimension D. As S_{3D} is a structure factor there is no intensity scaling factor: the scattered intensity induced by the fractal character will be directly proportional to that of the peak. As shown in the bottom illustration of Fig. 3b, r corresponds to the smallest flat section of the layers. Between r and Σ the layers are crumpled, whose distribution of radii of curvature follow a fractal exponent, while below r the layers can be considered as effectively flat. Σ is the fractal cut-off length, above which the fractal correlation vanishes, as illustrated in the bottom panel of Fig. 3b. Note that it does not necessarily correspond to a limited extension of the crumpled layers, it only means that their curvature will be aleatory above this length.

The refined fractal or topological D exponent for I_{waxs} in the CPC sample has been found to be $D = 2.6$, confirming the assumption that the layers are crumpled. The refinement with the Voigt profile indicates that the major contribution to the width of this peak is Lorentzian, which confirms it arises from a lamellar phase with distortion of the second kind as defined by Vonk [40], i.e. curved layers. The very good fit with the model indicates that no other source of scattering is needed to be considered to account for the SAXS scattering pattern of CPC soft carbon. As for graphite, there is thus no sign of presence of microporosity of any kind, the larger intensity scattered at intermediate range for CPC being

Table 1
Morphological parameters deduced from the component I_{porod} of the refinement of the full range SAXS patterns presented in Figs. 5–7.

Sample	$(\Delta SLD)^2_{sample}$ ($\times 10^{20}$ cm^{-4})	Porod (grains)		Porod (roughness)		S_{part} (m^2 g^{-1})	SSA_{BET} (N_2) (m^2 g^{-1})
		S_{macro} (m^2 g^{-1})	D_g (μm)	R_{rough} (nm)	S_{rough} (m^2 g^{-1})		
Graphite	363.7	6.5	0.4	4.9	2.6	9.1	17
CPC	385.3	1.8	1.5	4.5	1.7	3.5	3.98
GC	196.5	0	–	5.6	0.2	0.2	–
HC	218.9	0.4	9.3	3.9	0.6	1.0	34.0
AC	32.8	18.8	0.5	5.1	22.0	40.8	1538
CDC400	128.8	1.6	2.7	1.7	13.0	14.6	1023
CDC900	269.1	0.9	3.3	16.1	1.03	2.0	1534

Table 2
Structural and microstructural parameters deduced from the component I_{waxs} of the refinement of the full range SAXS patterns presented in Figs. 5–7.

Sample	Peak function					Form factor		
	d_{002} (nm)	W_G (nm^{-1})	W_L (nm^{-1})	W (nm^{-1})	ξ (nm)	R (nm)	Σ (nm)	D[b]
Graphite	0.338	0.397	0.14	0.48	13.87	∞	∞	–
CPC	0.346	0.990	1.33	1.89	1.50	0.093	1.06	2.64
GC	0.339	2.12	3.32	4.39	0.60¡	0.070	0.47	2.5
HC	0.351	0	8.44	8.44	0.24	0.444	0.199	2.5
AC	0.358	0	11.04	11.04	0.18	0.256	0.31	2.5
CDC400	0.375	9.97	0	9.97	–	–	–	–
CDC900	0.336	0.701	6.61	6.69	0.30	0.007	2.12	2.5
	0.340	0	1.21	1.22	1.64			

only due to the crumpling and curvature related distortion of its turbostratic structure.

3.5. Full range SAXS-WAXS analysis of glassy carbon, hard carbon and activated carbon

The full range SAXS-WAXS patterns of the microporous samples GC, HC and AC have been fitted using equation (1) and are shown in Fig. 6. Here I_{mp} is clearly needed in all samples in addition to I_{waxs} and to I_{Porod}. Interestingly, I_{mp} is very similar for the three samples, although differs in intensity and Q position. This signal is particularly evident for the GC sample, as exhibits a very small Porod scattering at low angle due to the fact that it is an unground bulk sample, as seen in Fig. S3. The intensity of GC is nearly constant for $Q < 1\ nm^{-1}$, and falls as Q^{-n} for larger Q, n close to 3.5, until it merges with the signal from the diffraction peak near $Q = 8\ nm^{-1}$. An exponent larger than 3 corresponds to a Porod's final slope regime due to the scattering by interfaces. This rapid and direct transition from constant intensity toward Q^{-n}, $n > 3$, reveals the presence of a single characteristic size in the nanometre range, indicating that the features at the origin of the scattered intensity in this range exhibit an aspect ratio close to 1. Indeed, an aspect ratio larger than 1 (rod shaped) would cause a Q^{-1} dependency in the intermediate range before transitioning to Q^{-4} at larger Q, and an aspect ratio lower than 1 (flat objects) would appear as Q^{-2} [43]; neither of the two being observed here. I_{mp} is qualitatively very close to the Teubner-Strey model, so that this model has been used to model the intensityI_{mp} for the three samples GC, HC and AC.

The expressions used for I_{Porod} and I_{waxs} are identical to those used for the CPC soft carbon sample in section 3, expressions (3) and (16), while for I_{mp} the Teubner-Strey model has been used, expression (8). The refined values of the morphological parameters related to I_{Porod}, I_{mp} and I_{waxs} extracted from the data are given in Tables 1–3, respectively.

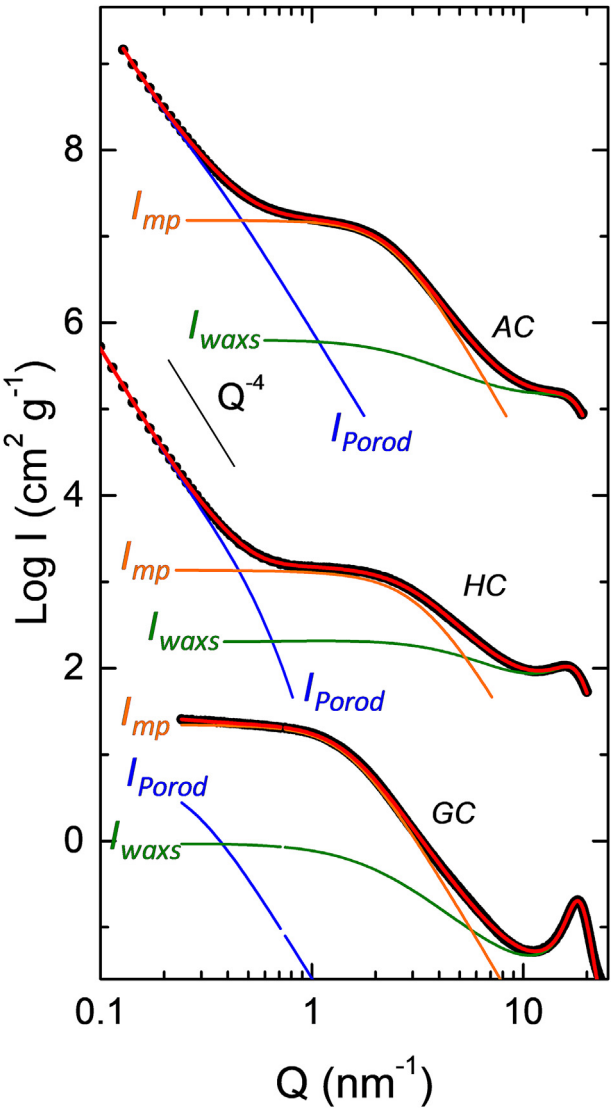

Fig. 6. Full range fit of microporous carbons AC, HC and GC. AC and HC intensities were shifted for clarity. Black symbols represent the experimental data, red curve represents the calculated pattern, the blue curve corresponds to the calculated I_{Porod}, the orange curve to the calculated I_{mp} and the green curve to the calculated I_{waxs}. (For interpretation of the references to colour in this figure legend, the reader is referred to the Web version of this article.)

3.6. Full range SAXS-WAXS analysis of carbide derived carbons

The full range SAXS-WAXS patterns of the CDC400 and CDC900 samples are shown in Fig. 7. Here I_{mp} has also been included, and for the CDC400 sample its shape is very similar to that of GC, HC and AC samples of Fig. 6, so it has been refined with the same Teubner-Strey model defined in expression (8). The expressions used for I_{Porod} and I_{waxs} are identical to those used for CPC, GC, HC and AC, defined respectively in expressions (3) and (16).

In the case of the CDC900 sample, a Q^{-n} dependency, n close to 1.8, is observed in the intermediate Q range for $Q < 2\ nm^{-1}$. Such Q

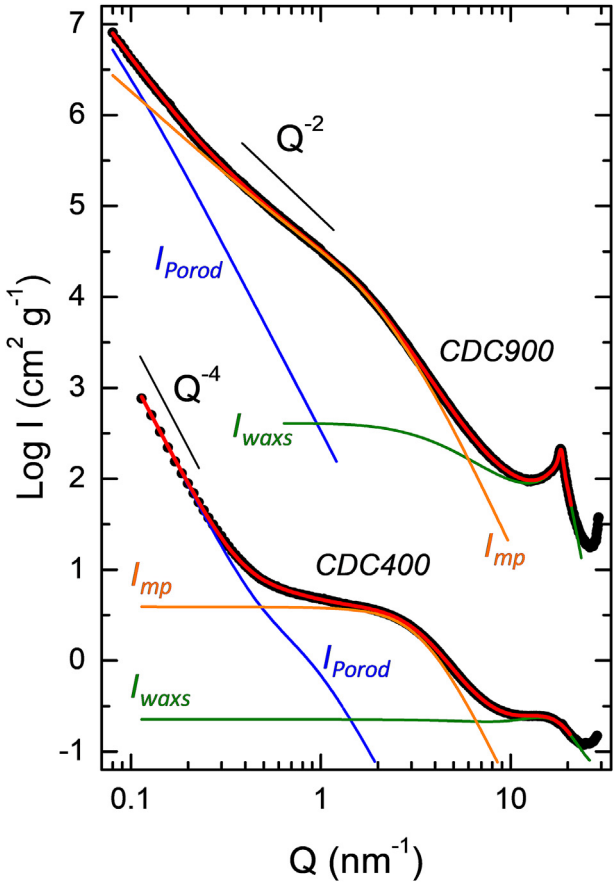

Fig. 7. Full range fit of CDC400 and CDC900 samples. CDC900 intensities were shifted for clarity. Black symbols represent the experimental data, red curve represents the calculated pattern, the blue curve corresponds to the calculated I_{Porod}, the orange curve to the calculated I_{mp} and the green curve to the calculated I_{waxs}. (For interpretation of the references to colour in this figure legend, the reader is referred to the Web version of this article.)

dependency cannot be modelled by the Teubner-Strey model, and therefore suggests the presence of pore-pore correlations for this sample. For this reason, the Teixeira model of fractal aggregates has been used for I_{mp}, as defined by expression (5). Two components had to be used for the proper modelling of the (002) peak of CDC900.

As can be appreciated in Fig. 7 the agreement between the best fit and the experimental data is very good in the whole Q range for this sample. The refined morphological parameters related to I_{Porod}, I_{waxs} and I_{mp} extracted from the data are given in Tables 1–3, respectively.

4. Discussion

As can be observed in Figs. 5–7, for all samples the agreement between the simulated curves and the experimental data is very good in the whole range of intensity and Q values, which validates the models used.

The morphological parameters extracted from the fit of the Porod scattering I_{Porod} are gathered in Table 1, and plotted in Fig. 8: S_{macro} is the macroscopic surface area of the powder, S_{rough} is the additional surface area related to the surface roughness in the mesoscopic range, and R_{rough} is the characteristic size of this surface roughness. It is interesting to note that the latter is close to 5 nm for all samples except the two CDCs. This seems to be a general feature of the layered sp^2 structure, probably related to the layer edges pointing at the surface of the particles. For the two non-porous samples, graphite and CPC soft carbon, $S_{grain} = S_{macro} + S_{rough}$ is found within the same order of magnitude than the B.E.T. surface area deduced from N_2 gas adsorption. The difference found for the graphite sample can be ascribed to the packing of the powder within the SAXS sample holder, while the samples are measured as free-standing powder in the gas adsorption measurement. Indeed, packing will generate particle-particle contact, reducing the effective macroscopic surface area S_{macro}. Since $S_{rug}/(S_{macro} + S_{rough})$ is larger for CPC soft carbon than for graphite, the possible effect of packing on S_{macro} should be less noticeable in CPC, because packing will affect S_{macro} but not S_{rough} which is related to mesoscale roughness. R_{rough} of CDC carbons differs strongly from the rest: it is close to 1.7 nm for CDC400, and 16 nm for CDC900. This can be ascribed to differences in the structure and microstructure of these carbons, as their method of preparation (chlorination of a carbide precursor, whose carbons atoms are sp^3 hybridized) is completely different from the other carbons, which are prepared form pyrolysis of organic precursors, thus mainly sp^2. As can be appreciated from Table 1, the grain size Dg that can be estimated from S_{macro} of the powdered samples is within the same order of magnitude than the average particle size measured from the SEM images of Fig. S2 and gathered in Table S2, which confirms S_{macro} as the surface area of the grains of the powder.

The structural and microstructural parameters extracted from I_{waxs} are gathered in Table 2, and a selection is plotted in Fig. 9. As can be seen from Fig. 9a, the width w of the (002) peak increases gradually for sp^2 carbons following the sequence graphite < CPC < GC < HC < AC. This is correlated with an increase of the Lorentzian weight in the peak profile, with HC and AC samples in the Lorentzian limit. As discussed in section 3.1, the broadening due to a curvature of the layers is expected to be Lorentzian, while for size broadening it is expected to have a strong Gaussian component. As a result, the fully Lorentzian (002) peak shape observed here for AC and HC points toward a broadening due to layer curvature rather than the presence of nanocrystallites. This challenges the traditional model of pseudo-graphitic nanocrystallites initially proposed by Franklin in 1951 [16] and still commonly used today to describe the microstructure of the non-graphitic carbons [13]. It is interesting to note that, while AC and HC can be both described with a nano-curved layered structure, these two carbons strongly differ in the surface porosity measured using N_2 as adsorbent, which is limited for HC and very high for AC. The nano-curved layered structure seems thus to be a general feature of non-graphitic carbons, independent on the degree of activation.

The characteristic sizes related to I_{waxs} are plotted in Fig. 9b. As introduced in expression (A3.38), ξ is the length above which the long-

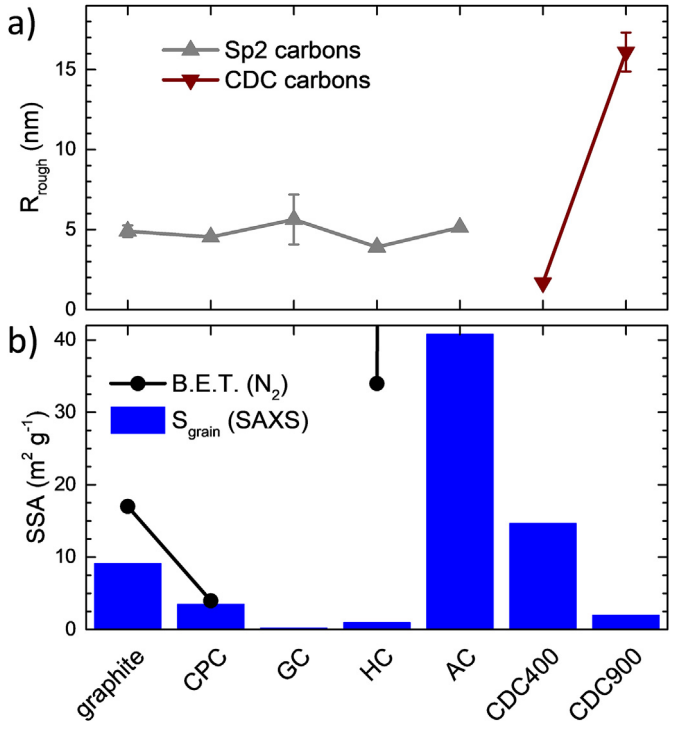

Fig. 8. Morphological refined parameters related to I_{Porod}. a) Characteristic R_{rough} size of the surface roughness of the particles. b) Surface area $S_{grain} = S_{macro} + S_{rough}$ measured from SAXS data (blue columns) and N_2 gas adsorption by the B.E.T. method (black circles). For samples AC, CDC400 and CDC900 the B.E.T. surface area is too large to appear in this graph and can be observed in Fig. 10. (For interpretation of the references to colour in this figure legend, the reader is referred to the Web version of this article.)

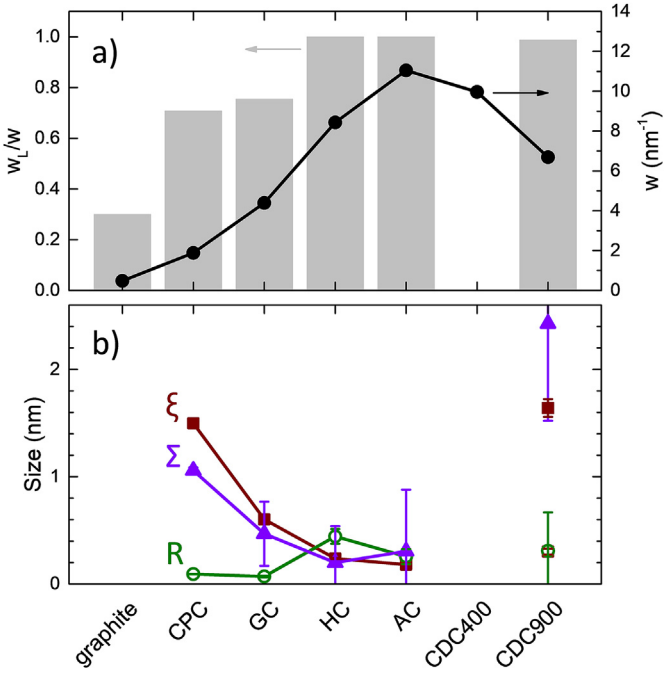

Fig. 9. Structural and microstructural refined parameters related to I_{waxs}. a) Full width at half maximum w of the (002) peak (black line) and Lorentzian width ratio w_L/w (grey columns). b) Characteristic sizes ξ, Σ and R. Note that for the CDC900 sample only the parameters of the more intense of the two contributions to the (002) peak are shown.

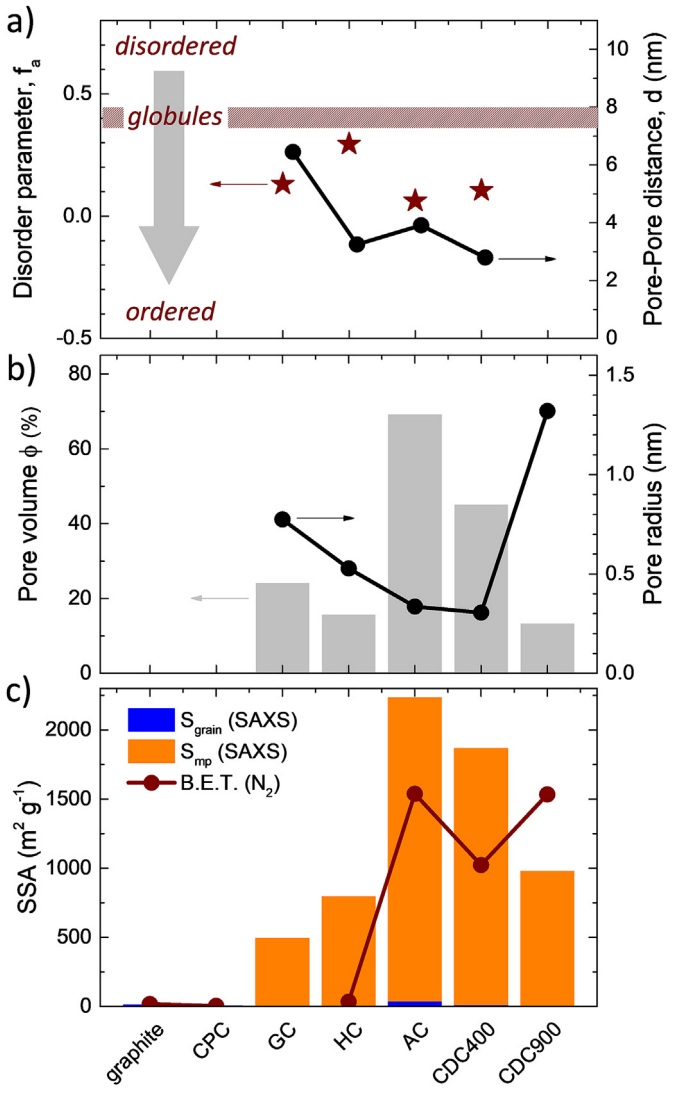

Fig. 10. Microstructural refined parameters related to I_{mp}. a) Disorder parameter (left axis) and pore-pore distance (right axis) of the microporous samples GC, HC, AC and CDC400. b) Micropore volume (left axis) and micropore radius (right axis). c) Specific surface area deduced from SAXS (columns) and gas adsorption (dark red circles). (For interpretation of the references to colour in this figure legend, the reader is referred to the Web version of this article.)

range order is lost, because of layer curvature, and is extracted from the FWHM, according to expression (A3.41). R corresponds to the length above which the layers cannot be considered as flat, and Σ is the length above which the fractal law vanishes. For CPC, a clear fractal character is observed, as discussed in section 3.4, with Σ about one order of magnitude larger than R. Following the sequence CPC > GC > HC, the length Σ drops quickly, and for HC and AC samples Σ and R have the same value (within error). All in all, one can interpret this evolution as a reduction of the average curvature radius following the sequence graphite > CPC > GC > HC > AC. Interestingly, ξ follows a very similar trend with Σ, which is to be expected: if the average curvature radius is reduced, the long-range order will be reduced. This is an additional indication that the peak broadening of non-graphitic carbons can be mainly ascribed to the layer curvature, without the need to consider a crystallite size reduction.

Again, the behaviour of the two CDC samples is very different from the rest of carbons. For the CDC400 carbon, the (002) peak was found to be described with a pure Gaussian function. Although this result should be taken with caution, since the (002) peak of CDC400 is very weak, this suggests that other factors reducing crystallinity, such as effective crystallite size contribute to the (002) peak broadening. This suggests that the structure is probably too disordered to be described as layered, which could be a consequence of some sp^3 carbon remaining in the structure. On the contrary, the (002) peak of CDC900 sample is mainly Lorentzian, with a width that is smaller than for non-graphitic carbons HC and AC. Conversely Σ is larger than that of all the other non-graphitic carbons, which suggests that the structure of this carbon is closer to that of a sp^2 carbon, in agreement with the second narrow contribution to the (002) peak whose position is close to that of graphite.

Table 3
Morphological parameters of the microporosity deduced from the component I_{mp} of the refinement of the full range SAXS patterns presented in Figs. 6 and 7. ΔSLD is the contrast of scattering length density between the carbon matrix and the pores, d is the average pore-pore distance, ξ the length beyond which the order is lost, f_a the order parameter, r the micropore radius, S_{mp} the micropore surface area and φ the volume fraction occupied by the micropores.

Sample	$(\Delta SLD)^2_C$ ($x10^{20}$ cm^{-4})	d (nm)	ξ (nm)	f_a	r (nm)	S_{mp} (m^2 g^{-1})	φ (%)
GC	341.0	6.45	0.90	0.13	0.77	493	24.1
HC	307.2	3.25	0.38	0.29	0.53	792	15.6
AC	336.9	3.91	0.59	0.06	0.34	2189	69.1
CDC400	426.2	2.80	0.40	0.10	0.31	1851	45.0
CDC900	357.7	–	–	–	1.32	975	13.3

The morphological parameters related to the micropore scattering I_{mp} of the microporous carbons GC, HC, AC, CDC400 and CDC900 are gathered in Table 3, and a selection is plotted in Fig. 10. The surface area of the microporous samples (GC, HC, AC, CDC400 and CDC900) appears in the range 500–2200 m^2/g, see Fig. 10c, which is 1–2 orders of magnitude higher than the surface area deduced from I_{Porod} shown in Fig. 8b. The average pore size is found in the range 1–2 nm, thus confirming their microporous character. The disorder parameter f_a for the samples analysed using the Teubner-Strey model is found in the range 0.1–0.3, see Fig. 10a, which is smaller than for randomly spread globule-shaped pores, suggesting that the pores exhibit some degree of short-range pore-pore ordering. The pore-pore distance is found in the range 3–7 nm and is shown to be correlated with pore size, see Fig. 10a. All in all, for these 5 samples the pore structure can be described as a sponge-like microstructure made of pores with aspect ratio close to 1, which, although randomly spread in the carbon matrix, exhibit some degree of short-range order suggesting repulsive type correlations. It should be noted that a pore aspect ratio close to 1 is more compatible with curved layers and thus reinforces the model, as slit pores would require parallel layers. This has important consequence for the analysis of the porosity from e.g. gas adsorption. Indeed, DFT-based analysis of gas adsorption isotherms generally assume slit shaped pores, which have a different surface area to volume ratio compared to spheroid pores. SAXS can thus be used to extract pore-shapes to be used for example as input for modelling studies or gas adsorption analysis methods. A very good example is the recent work of Prehal et al. who performed Monte Carlo simulation of the pore structure on the basis of the input given by SAXS [51].

As can be observed in Table 3 and Fig. 10b, the pore volume of the non-activated GC and HC samples is found close to 20%, with a surface area of 493 m^2/g for GC and 792 m^2/g for HC. This might appear surprising at first sight since GC is known to exhibit zero B.E.T. SSA and HC has a rather modest N_2 B.E.T. SSA of 30 m^2/g. However X-rays can penetrate to the bulk of particles, and therefore the measured SAXS pore volume includes bulk pores that are not accessible to gas adsorption.

The pore volume is significantly larger (50–70%) for samples exhibiting large N_2 B.E.T. SSA: AC, CDC400 and CDC900, with 2190, 1850 and 980 m^2/g, respectively. For AC and CDC400 samples the SAXS pore volume is 30–40% larger than the N_2 B.E.T. SSA, which indicates that these carbons exhibit a non-negligible amount of micropores that are not

accessible to N_2. In terms of pore volume, this would correspond to a volume fraction of non-accessible pores of about 20%, which is close to that of GC and HC. This suggests that a pore volume fraction of 20% that is not accessible to N_2 is a common feature of non-graphitizable carbons, independently on their level of activation. In the case of CDC900 S_{mp} is 30% lower than N_2 B.E.T. SSA, which is rather surprising because pores may not be accessible to N_2, but they should scatter X-rays. A possible explanation is the presence of impurities that have been detected in the 2D SAXS patterns in form of diffraction spots, possibly due to some trace of carbide precursor, or contamination during the synthesis. Although it has not been possible to quantify nor identify these impurities, if they are of inorganic nature they might significantly affect the transmission and thus the estimation of the powder density from expression (A1.19), by which the SAXS intensity is then normalized.

The large surface area detected by SAXS for GC and HC samples can thus be ascribed to porosity that is not accessible to N_2, possibly because it is totally closed, or connected to the surface by paths that are too narrow or tortuous to allow N_2 diffusion. It is important to note that, as can be seen in Fig. S4, the measurement time for the low-pressure points of the N_2 isotherm of HC reached tens of hours, which is extremely high compared to the few minutes typically needed for active carbon. When the N_2 isotherm was performed with a less drastic equilibrium condition, near zero surface area was detected. This is consistent with the micropore closure mechanism proposed by Dahn's group in the 90's to explain the general reduction of N_2 surface area while increasing the synthesis temperature [51–54].

This is a very important parameter for M-ion batteries (M = Li, Na, K, etc.) since the redox reaction potential of carbon materials lies below the stability limit of the commonly used electrolytes causing electrolyte decomposition, and therefore irreversible charge consumption will occur until the surface is finally passivated by the Solid Electrolyte Interphase (SEI) formation. On the other side, it is well-known that microporosity allows to extend the Li or Na uptake of non-graphitic carbons, see e.g. Refs. [18,33,34,55,56], although the actual mechanism is still under intense debate. An ideal non-graphitic carbon anode would thus have to combine high internal micropore volume with closed external surface area, limiting the analytical capacity of gas adsorption to decipher charge storage mechanisms and support internal microporosity optimization. However, in most studies related to hard carbon for Li or Na batteries where SAXS data are used the intensity is not calibrated, which hinders the quantification of bulk micro-porosity. The present study demonstrates that intensity calibration is possible even with a lab-scale instrument, and unveils that the surface area of the closed porosity in hard carbon can be of the same order of magnitude than open porosity of active carbons. An intensity-calibrated SAXS instrument therefore represents an extremely useful tool to further understand and optimize non-graphitic microporous carbons for energy applications. Moreover, SAXS has the benefit of being compatible with *in-situ* or *operando* measurements of samples in electrochemical cells, as it is a non-destructive technique. While only a few reports can be found for in-situ or operando SAXS, see e.g. Refs. [30,48], it has an enormous potential to study the charge storage mechanism, either for battery application (closed porosity) or supercapacitor application (open porosity).

5. Conclusion

Using a combination of models to describe the different components of experimental carbon SAXS patterns (I_{Porod}, I_{mp} and I_{waxs}), combined with an intensity calibrated instrument, an accurate description of atomic and pore structures has been obtained. Such description allows quantifying relevant concepts like the surface area and volume fraction of inaccessible pores, the shape of the pores (aspect ratio), or pore organization (pore-pore correlations or ordering) that are likely to have a strong impact in charge storage mechanisms and are not considered to date. It has been shown that microporous carbons (AC, GC, HC, CDCs) univocally require the contribution of the pore structure for a full description of their X-ray pattern, and therefore SAXS represents a unique tool to measure buried porosity. The use of the full 2θ SAXS-WAXS range has also allowed to accurately determine the Lorentzian contribution to the (002) peak broadening, which has unveiled the fact that non-graphitic carbons like AC and HC exhibit a nano-curved layered structure, a description that clearly indicates that the widely used traditional models to describe these carbons need to be reviewed.

Acknowledgements

We acknowledge the financial support of the Ministerio de Economía y Competitividad through AffINIty (ENE2016-75242-R) and ION-STORE grants (ENE2016-81020-R), and the Basque Government through ELKARTEK project CICE17. We also gratefully acknowledge the support of Brahim Orayech for the HC sample, and BL11-NCD beamline at ALBA Synchrotron and ALBA staff for the measurement of the GC sample.

Appendix A. Supplementary data

Supplementary data to this article can be found online at https://doi.org/10.1016/j.ensm.2019.05.007.

References

[1] A. Hirsch, The era of carbon allotropes, Nat. Mater. 9 (2010) 868–871, https://doi.org/10.1038/nmat2885.
[2] Z. Lin, E. Goikolea, A. Balducci, K. Naoi, P.L. Taberna, M. Salanne, G. Yushin, P. Simon, Materials for supercapacitors: when Li-ion battery power is not enough, Mater. Today 21 (2018) 419–436, https://doi.org/10.1016/j.mattod.2018.01.035.
[3] M. Winter, J.O. Besenhard, M.E. Spahr, P. Novák, Insertion electrode materials for rechargeable lithium batteries, Adv. Mater. 10 (1998) 725–763, https://doi.org/10.1002/(SICI)1521-4095(199807)10:10<725::AID-ADMA725>3.0.CO;2-Z.
[4] X. Dou, I. Hasa, D. Saurel, C. Vaalma, L. Wu, D. Buchholz, D. Bresser, S. Komaba, S. Passerini, Hard carbons for sodium-ion batteries: structure, analysis, sustainability, and electrochemistry, Mater. Today (2019), https://doi.org/10.1016/j.mattod.2018.12.040.
[5] Z. Jian, W. Luo, X. Ji, Carbon electrodes for K-ion batteries, J. Am. Chem. Soc. 137 (2015) 11566–11569, https://doi.org/10.1021/jacs.5b06809.
[6] X. Ji, L.F. Nazar, Advances in Li–S batteries, J. Mater. Chem. 20 (2010) 9821–9826, https://doi.org/10.1039/B925751A.
[7] J. Christensen, P. Albertus, R.S. Sanchez-Carrera, T. Lohmann, B. Kozinsky, R. Liedtke, J. Ahmed, A. Kojic, A critical review of Li/air batteries, J. Electrochem. Soc. 159 (2011) R1–R30, https://doi.org/10.1149/2.086202jes.
[8] J.-S. Lee, S.T. Kim, R. Cao, N.-S. Choi, M. Liu, K.T. Lee, J. Cho, Metal–air batteries with high energy density: Li–air versus Zn–air, Adv. Energy Mater. 1 (2011) 34–50, https://doi.org/10.1002/aenm.201000010.
[9] I. Landa-Medrano, C. Li, N. Ortiz-Vitoriano, I. Ruiz de Larramendi, J. Carrasco, T. Rojo, Sodium–oxygen battery: steps toward reality, J. Phys. Chem. Lett. 7 (2016) 1161–1166, https://doi.org/10.1021/acs.jpclett.5b02845.
[10] Q. Xu, T. Kobayashi, Advanced Materials for Clean Energy, CRC Press, 2015.
[11] S. Flandrois, B. Simon, Carbon materials for lithium-ion rechargeable batteries, Carbon 37 (1999) 165–180, https://doi.org/10.1016/S0008-6223(98)00290-5.
[12] J.R. Dahn, T. Zheng, Y. Liu, J.S. Xue, Mechanisms for lithium insertion in carbonaceous materials, Science 270 (1995) 590–593, https://doi.org/10.1126/science.270.5236.590.
[13] R.E. Franklin, The structure of graphitic carbons, Acta Crystallogr. 4 (1951) 253–261, https://doi.org/10.1107/S0365110X51000842.
[14] F.C. Cowlard, J.C. Lewis, Vitreous carbon — a new form of carbon, J. Mater. Sci. 2 (1967) 507–512, https://doi.org/10.1007/BF00752216.
[15] S. Mrozowski, Semiconductivity and diamagnetism of polycrystalline graphite and condensed ring systems, Phys. Rev. 85 (1952) 609–620, https://doi.org/10.1103/PhysRev.85.609.
[16] R.E. Franklin, Crystallite growth in graphitizing and non-graphitizing carbons, Proc. R. Soc. Lond. Math. Phys. Eng. Sci. 209 (1951) 196–218, https://doi.org/10.1098/rspa.1951.0197.
[17] J.J. Kipling, J.N. Sherwood, P.V. Shooter, N.R. Thompson, The pore structure and surface area of high-temperature polymer carbons, Carbon 1 (1964) 321–328, https://doi.org/10.1016/0008-6223(64)90286-6.
[18] D. Saurel, B. Orayech, B. Xiao, D. Carriazo, X. Li, T. Rojo, From charge storage mechanism to performance: a roadmap toward high specific energy sodium-ion batteries through carbon anode optimization, Adv. Energy Mater. 8 (2018) 1703268, https://doi.org/10.1002/aenm.201703268.
[19] Y. Nishi, The development of lithium ion secondary batteries, Chem. Rec. 1 (2001) 406–413, https://doi.org/10.1002/tcr.1024.

[20] R. Fong, U. von Sacken, J.R. Dahn, Studies of lithium intercalation into carbons using nonaqueous electrochemical cells, J. Electrochem. Soc. 137 (1990) 2009–2013, https://doi.org/10.1149/1.2086855.
[21] M.M. Doeff, Y. Ma, S.J. Visco, L.C.D. Jonghe, Electrochemical insertion of sodium into carbon, J. Electrochem. Soc. 140 (1993) L169–L170, https://doi.org/10.1149/1.2221153.
[22] X. Xia, M.N. Obrovac, J.R. Dahn, Comparison of the reactivity of NaxC6 and LixC6 with non-aqueous solvents and electrolytes, Electrochem. Solid State Lett. 14 (2011) A130–A133, https://doi.org/10.1149/1.3606364.
[23] D.A. Stevens, J.R. Dahn, High capacity anode materials for rechargeable sodium-ion batteries, J. Electrochem. Soc. 147 (2000) 1271–1273, https://doi.org/10.1149/1.1393348.
[24] S. Komaba, W. Murata, T. Ishikawa, N. Yabuuchi, T. Ozeki, T. Nakayama, A. Ogata, K. Gotoh, K. Fujiwara, Electrochemical Na insertion and solid electrolyte Interphase for hard-carbon electrodes and application to Na-ion batteries, Adv. Funct. Mater. 21 (2011) 3859–3867, https://doi.org/10.1002/adfm.201100854.
[25] G. Hasegawa, K. Kanamori, N. Kannari, J. Ozaki, K. Nakanishi, T. Abe, Studies on electrochemical sodium storage into hard carbons with binder-free monolithic electrodes, J. Power Sources 318 (2016) 41–48, https://doi.org/10.1016/j.jpowsour.2016.04.013.
[26] P.J.F. Harris, Structure of non-graphitising carbons, Int. Mater. Rev. 42 (1997) 206–218, https://doi.org/10.1179/imr.1997.42.5.206.
[27] F. Legrain, J. Sottmann, K. Kotsis, S. Gorantla, S. Sartori, S. Manzhos, Amorphous (glassy) carbon, a promising material for sodium ion battery anodes: a combined first-principles and experimental study, J. Phys. Chem. C 119 (2015) 13496–13501, https://doi.org/10.1021/acs.jpcc.5b03407.
[28] F. Beguin, E. Frackowiak, E. Frackowiak, Carbons for Electrochemical Energy Storage and Conversion Systems, CRC Press, 2009, https://doi.org/10.1201/9781420055405.
[29] L. Weinstein, R. Dash, Supercapacitor carbons, Mater. Today 16 (2013) 356–357, https://doi.org/10.1016/j.mattod.2013.09.005.
[30] J. Chmiola, G. Yushin, Y. Gogotsi, C. Portet, P. Simon, P.L. Taberna, Anomalous increase in carbon capacitance at pore sizes less than 1 nanometer, Science 313 (2006) 1760–1763, https://doi.org/10.1126/science.1132195.
[31] C. Largeot, C. Portet, J. Chmiola, P.-L. Taberna, Y. Gogotsi, P. Simon, Relation between the ion size and pore size for an electric double-layer capacitor, J. Am. Chem. Soc. 130 (2008) 2730–2731, https://doi.org/10.1021/ja7106178.
[32] J.E. Parmeter, D.R. Tallant, M.P. Siegal, Thermal stability studies of diamond-like carbon films, MRS Online Proc. Libr. Arch. 349 (1994), https://doi.org/10.1557/PROC-349-513.
[33] C. Bommier, T.W. Surta, M. Dolgos, X. Ji, New mechanistic insights on Na-ion storage in nongraphitizable carbon, Nano Lett. 15 (2015) 5888–5892, https://doi.org/10.1021/acs.nanolett.5b01969.
[34] D.A. Stevens, J.R. Dahn, The mechanisms of lithium and sodium insertion in carbon materials, J. Electrochem. Soc. 148 (2001) A803–A811, https://doi.org/10.1149/1.1379565.
[35] H. Marsh, F. Rodriguez-Reinoso, Activation Processes (Thermal or Physical), Act. Carbon, first ed., Elsevier Sci. Oxf, UK, 2006.
[36] L.L. Ban, D. Crawford, H. Marsh, Lattice-resolution electron microscopy in structural studies of non-graphitizing carbons from polyvinylidene chloride (PVDC), J. Appl. Crystallogr. 8 (1975) 415–420, https://doi.org/10.1107/S0021889875010904.
[37] A. Yoshida, Y. Kaburagi, Y. Hishiyama, Microtexture and magnetoresistance of glass-like carbons, Carbon 29 (1991) 1107–1111, https://doi.org/10.1016/0008-6223(91)90027-G.
[38] S.J. Townsend, T.J. Lenosky, D.A. Muller, C.S. Nichols, V. Elser, Negatively curved graphitic sheet model of amorphous carbon, Phys. Rev. Lett. 69 (1992) 921–924, https://doi.org/10.1103/PhysRevLett.69.921.
[39] P.J.F. Harris, S.C. Tsang, High-resolution electron microscopy studies of non-graphitizing carbons, Philos. Mag. A 76 (1997) 667–677, https://doi.org/10.1080/01418619708214028.
[40] C.G. Vonk, The small-angle scattering of distorted lamellar structures, J. Appl. Crystallogr. 11 (1978) 541–546, https://doi.org/10.1107/S0021889878013837.
[41] B.R. Pauw, Everything SAXS: small-angle scattering pattern collection and correction, J. Phys. Condens. Matter 25 (2013) 383201, https://doi.org/10.1088/0953-8984/25/38/383201.
[42] NIST: X-Ray Mass Attenuation Coefficients - Carbon, Graphite, (n.d.), https://physics.nist.gov/PhysRefData/XrayMassCoef/ElemTab/z06.html. (Accessed 14 February 2019).
[43] G. Porod, General Theory, Small Angle X-Ray Scatt, 1982. http://inis.iaea.org/Search/search.aspx?orig_q=RN:16012432. (Accessed 15 February 2019).
[44] J. Teixeira, Small-angle scattering by fractal systems, J. Appl. Crystallogr. 21 (1988) 781–785, https://doi.org/10.1107/S0021889888000263.
[45] K.-V. Schubert, R. Strey, S.R. Kline, E.W. Kaler, Small angle neutron scattering near Lifshitz lines: transition from weakly structured mixtures to microemulsions, J. Chem. Phys. 101 (1994) 5343–5355, https://doi.org/10.1063/1.467387.
[46] M. Teubner, R. Strey, Origin of the scattering peak in microemulsions, J. Chem. Phys. 87 (1987) 3195–3200, https://doi.org/10.1063/1.453006.
[47] P. Debye, A.M. Bueche, Scattering by an inhomogeneous solid, J. Appl. Phys. 20 (1949) 518–525, https://doi.org/10.1063/1.1698419.
[48] Y. Kantor, M. Kardar, D.R. Nelson, Statistical mechanics of tethered surfaces, Phys. Rev. Lett. 57 (1986) 791–794, https://doi.org/10.1103/PhysRevLett.57.791.
[49] A.S. Balankin, R.C.M. de Oca, D.S. Ochoa, Intrinsically anomalous self-similarity of randomly folded matter, Phys. Rev. E. 76 (2007), https://doi.org/10.1103/PhysRevE.76.032101.
[50] P.A. Marsh, A. Voet, T.J. Mullens, L.D. Price, Quantitative micrography of carbon black microstructure, Carbon 9 (1971) 797–805, https://doi.org/10.1016/0008-6223(71)90013-3.
[51] C. Prehal, C. Koczwara, N. Jäckel, A. Schreiber, M. Burian, H. Amenitsch, M.A. Hartmann, V. Presser, O. Paris, Quantification of ion confinement and desolvation in nanoporous carbon supercapacitors with modelling and *in situ* X-ray scattering, Nat. Energy 2 (2017) 16215, https://doi.org/10.1038/nenergy.2016.215.
[52] E. Buiel, J.R. Dahn, Reduction of the irreversible capacity in hard-carbon anode materials prepared from sucrose for Li-ion batteries, J. Electrochem. Soc. 145 (1998) 1977–1981, https://doi.org/10.1149/1.1838585.
[53] E.R. Buiel, A.E. George, J.R. Dahn, Model of micropore closure in hard carbon prepared from sucrose, Carbon 37 (1999) 1399–1407, https://doi.org/10.1016/S0008-6223(98)00335-2.
[54] J.R. Dahn, W. Xing, Y. Gao, The “falling cards model” for the structure of microporous carbons, Carbon 35 (1997) 825–830, https://doi.org/10.1016/S0008-6223(97)00037-7.
[55] R. Morita, K. Gotoh, M. Fukunishi, K. Kubota, S. Komaba, N. Nishimura, T. Yumura, K. Deguchi, S. Ohki, T. Shimizu, H. Ishida, Combination of solid state NMR and DFT calculation to elucidate the state of sodium in hard carbon electrodes, J. Mater. Chem. A. 4 (2016) 13183–13193, https://doi.org/10.1039/C6TA04273B.
[56] J.M. Stratford, P.K. Allan, O. Pecher, P.A. Chater, C.P. Grey, Mechanistic insights into sodium storage in hard carbon anodes using local structure probes, Chem. Commun. 52 (2016) 12430–12433, https://doi.org/10.1039/C6CC06990H.